Journal of Geosciences, 59 (2014), 23–40 DOI: 10.3190/jgeosci.161

Original paper

The camptonites in the multiple intrusion of Platja Fonda (Girona, NE Spain): mechanisms of intrusion and geochemistry

Sergi ESTEVE[1*], Pere ENRIQUE[1], Gumer GALÁN[2]

[1] *Departament de Geoquímica, Petrologia i Prospecció Geològica, Universitat de Barcelona, Martí i Franqués s/n, 28028 Barcelona, Spain; ecce.pecto@gmail.com*

[2] *Departament de Geologia, Universitat Autònoma de Barcelona, Edifici C (sur), 08193 Bellaterra–Barcelona, Spain*

[*] *Corresponding author*

The camptonites of Platja Fonda are intrusive into Cambro–Ordovician metasediments and late Variscan granitoids. They appear as decimetre to centimetre thick sub-horizontal dykes following a fracture system, with dilation nearly orthogonal to their strike. The largest dykes have zoned structure, with chilled margins at both borders grading to porphyritic camptonites towards the centre, whereas the latest thinner dykes are intrusive into the porphyritic camptonites and their texture is almost aphyric. The macrocrysts of the porphyritic camptonites are interpreted as phenocrysts according to their chemistry and conditions of formation with respect to the crystals in the groundmass. They are mainly of kaersutite and of subordinate diopside–augite. Whole-rock major-element compositions reveal the existence of two types of camptonites: the predominant, sodi–potassic and the subordinate, slightly potassic. Other geochemical differences between the two types are minimal. The potassic camptonites are found as isolated dykes, but the potassic tendency exists in the latest thinner dykes that cross-cut earlier sodi–potassic camptonites and show small amount of normative leucite. Both types do not seem to be related by fractional crystallization and could represent slightly different alkaline melts, which would have been formed by partial melting of a metasomatized mantle. Increasing participation of the incongruent breakdown of calcic amphibole and phlogopite during the genesis of the most potassic camptonites is suggested. These camptonites in general, and specifically the potassic ones, have the lowest SiO_2, the highest CaO and the lowest Mg numbers of all known camptonites in the Catalan Coastal Ranges.

Keywords: camptonites, intrusion mechanism, petrography, mineralogy, geochemistry
Received: 29 May 2013; accepted: 24 February 2014; handling editor: F. V. Holub

1. Introduction

Late Variscan granitoids in the Catalan Coastal Ranges (NE Spain) (Fig. 1a) are cross-cut by several types of lamprophyres in their northeastern outcrops. So far, two different types of lamprophyres have been described according to their strike: a swarm of sub-vertical dykes of up to 1 m in thickness, trending W–E to NW–SE, and less frequent sub-horizontal dykes or sills, up to 2 m thick, cross-cutting locally the previous ones and trending N–S to NW–SE (Enrique 2009). Earlier studies on these rocks classified the two types as spessartites and camptonites, respectively (San Miguel de la Cámara 1936; San Miguel Arribas 1952). However, bostonites also exist (Enrique 2009) in sub-vertical dykes, nearly parallel to spessartites, but cross-cutting them (Enrique et al. 2012). In fact, some of the traditionally considered spessartites could be already transitional between subalkaline and alkaline lamprophyres, according to Ubide et al. (2010). The first specific research on the camptonites was focused on their mineralogy, petrology and whole-rock major-element compositions (Velde and Tournon 1970). Later studies developed further these issues (Ubide et al. 2008) along with the trace-element geochemistry and the detailed internal structure of individual sills (Ubide et al. 2009, 2012). Ubide et al. (2009, 2012) focused on a zoned narrow sill located further south than the outcrops represented in Fig. 1b. It shows porphyritic texture at the centre and is interpreted as having formed from a single pulse of magma, with gravitational settling of antecrysts towards the centre. However, in this area, camptonitic lamprophyres also appear forming multiple intrusions, representing distinct, though nearly coetaneous, magmatic pulses.

Our paper is focused on one of these multiple intrusions, aiming to assess the mechanisms of emplacement, to unravel the compositional variation between the sequential camptonitic pulses, and to shed light on the nature of magmatic processes at depth. For such a purpose, mineral and whole-rock major-element compositions, along with whole-rock trace element geochemistry, are used. Our results indicate that there are two types of camptonites in this multiple intrusion, one sodi–potassic and the other slightly potassic. Both types may have resulted from partial melting of a metasomatized mantle, with garnet as a residual phase, whereby the incongruent breakdown of amphibole and phlogopite would have

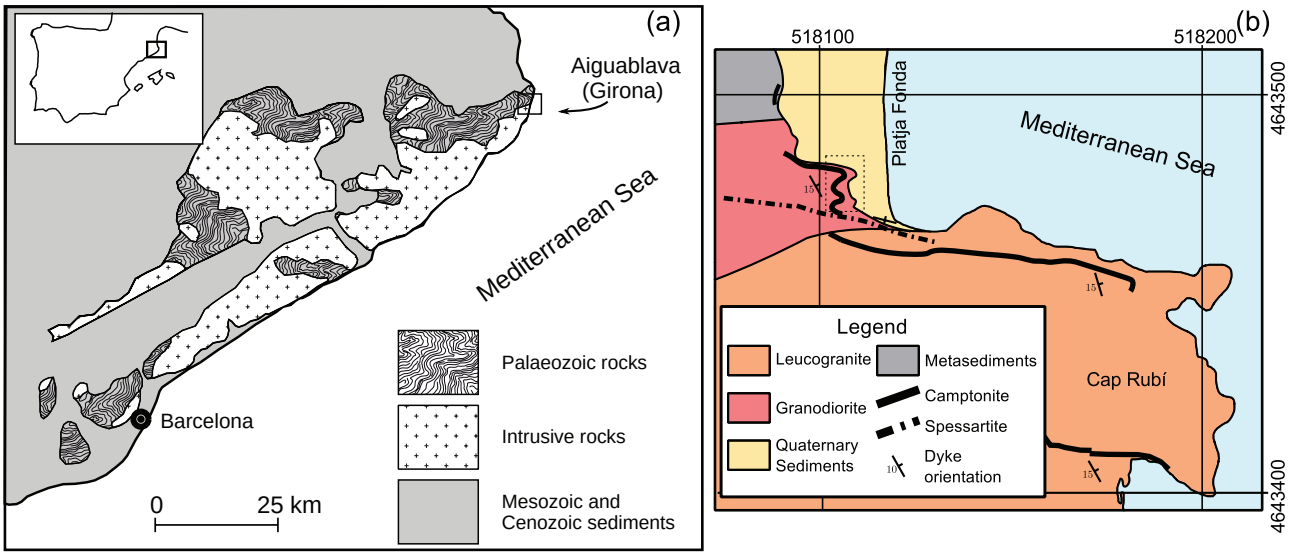

Fig. 1a – Location of the lamprophyric outcrops in the Catalan Coastal Ranges. **b** – Geological map of the southern area of Platja Fonda. UTM31N-ED50 coordinates.

been more significant during the genesis of the potassic camptonites. A regional compositional variation between the camptonites from north to south is also observed, in the Catalan Coastal Ranges.

2. Geological setting

The studied rocks crop out at the southeastern limit of Platja Fonda, near Aiguablava (Girona) (Fig. 1a–b). The wall-rocks are metasediments of Cambro–Ordovician age and late Variscan post-tectonic granitoids of the Catalan Coastal Ranges batholith (Enrique 1990). The metasediments are phyllites and quartz–feldspar hornfelses formed during the Variscan regional and contact metamorphism, the latter caused by the intrusion of the granitoids. In this area, the granitoids are porphyritic biotite granodiorites and biotite leucogranites of Aiguablava (Fig. 1b). Dating of biotite with the Ar–Ar method provided ages of 288 ± 3 Ma for the granodiorites and 287 ± 3 Ma for the leucogranites (Ferrés 1998). Swarms of lamprophyric dykes are especially common in this part of the batholith, following a pre-existing joint system in the granitoids (San Miguel Arribas 1952; Martínez-Poza et al. 2012). Field relationships indicate that spessartites were the first lamprophyre generation, followed by bostonite and camptonite dykes (Enrique et al. 2012). The spessartite lamprophyres are the most widespread. Their whole-rock K–Ar age is Late Permian (253 ± 5 Ma; Losantos et al. 2000), while the available age for a nearby camptonite is Late Cretaceous (76.0 ± 0.3 Ma determined on kaersutite with the Ar–Ar method; Solé et al. 2003). This latter age is slightly younger than the K–Ar age of the alkaline magmatism in the North Pyrenean Rift Zone (113–85 Ma according to Montigny et al. 1986), which also included lamprophyres (monchiquites and sannaites) (Azambre et al. 1992). In this coastal zone, the camptonites form sub-horizontal dykes or sills, among which those of Platja Fonda are the northernmost outcrops. All these coastal outcrops of camptonites represent most likely parts of the same intrusion (Ubide et al. 2008; Enrique 2009).

3. Analytical methods

Mineral analyses were performed with a Cameca SX50 electron microprobe at the "Serveis Cientificotècnics" of the University of Barcelona. Beam current and acceleration voltage were 15 nA and 20 kV, respectively. Standards were both natural and synthetic, and the counting time was 20–30 s depending on the element analysed. The correction method used was PAP (Pouchou and Pichoir 1984). As an example, precision for major elements in amphibole was better than 3% (1σ), except for K (< 5%), Na (< 10%) and Mn (< 40%). Precision for Cr was much worse (100%). Representative analyses of minerals are included in Tabs 1–4.

Whole-rock major- and trace-element compositions were determined at the ALS-Group laboratories, Canada (*http://www.alsglobal.com*). After fusion with lithium metaborate and then three steps of acid digestion (four in the case of base metals), major elements along with base metals were determined by Agilent 725 ICP-OES. The other trace elements, rare earth elements (REE) included, were analysed by Agilent 7700x ICP-MS. Precision estimates for major and trace elements based on replicated measurements of standard reference materials are included in Tab. 5. These were AMIS0085, SY-4 for major

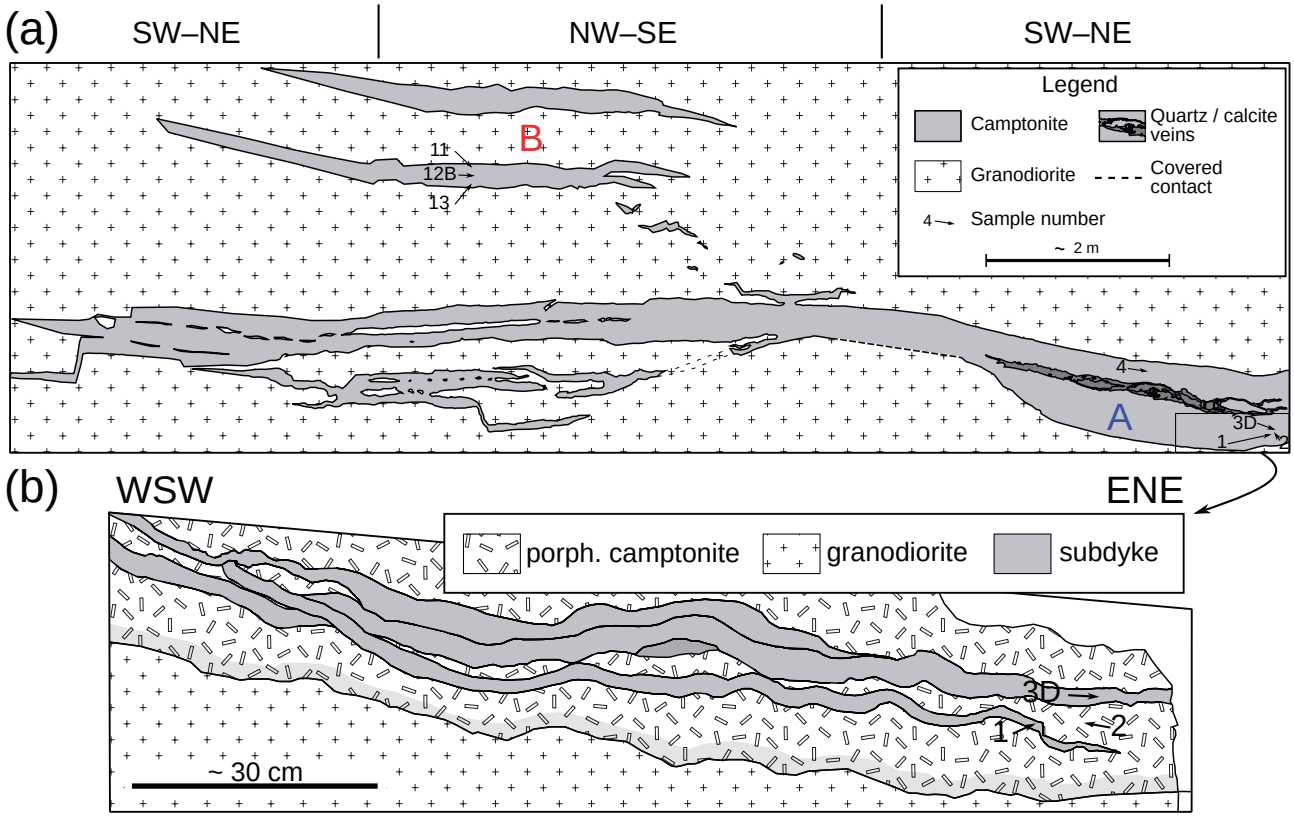

Fig. 2a – General sketch of the multiple intrusion of Platja Fonda showing the two parts, A and B. The rectangular area corresponds to the detailed cross-section in **b.** Location of studied samples is indicated in both figures.

and minor elements, LKSD-2 for the loss on ignition, OREAS-104 for most trace elements and GMB908-5 for Co, Cu, Mo, Ni, Pb, Sc and Zn.

4. Internal form and structure of the multiple intrusion

The Platja Fonda intrusion is formed by centimetre to decimetre thick sub-horizontal dykes (or sills) (Fig. 2a), intruding either the late Variscan porphyritic biotite granodiorite or the Cambro–Ordovician metasediments. The whole intrusion shows sharp and irregular contacts, and chilled margins at both sides. Wall-rock xenoliths are rare. One of the sills is discontinuous, marked B in Fig. 2a, *c.* 25 cm thick and with aphyric texture at the chilled margins grading to porphyritic one inwards (Fig. 3a). Both chilled margins enclose a thin layer of carbonate amygdales. Crystals of uncertain origin, concentrated in the centre and

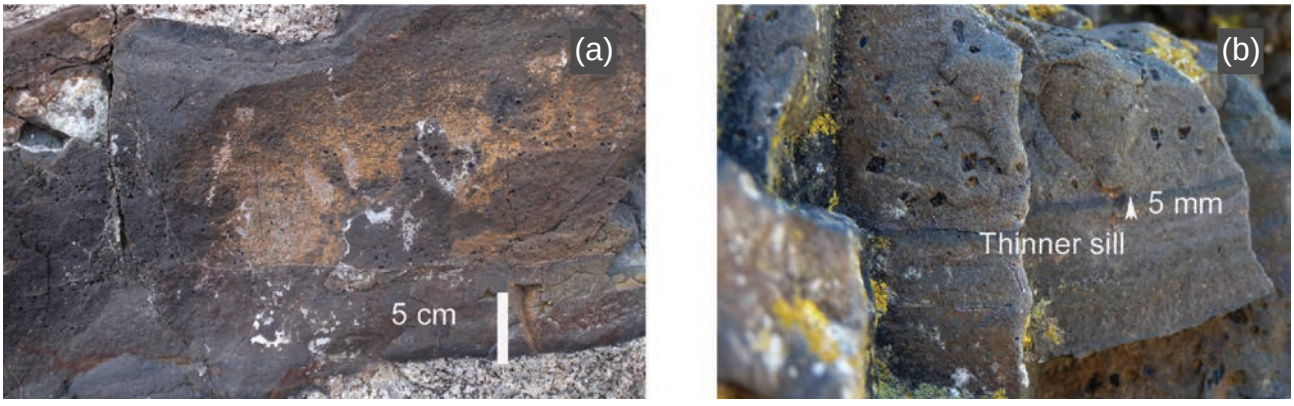

Fig. 3a – Structure of the isolated sill B in Fig. 2a. **b** – Thinner sills of part A, one of them with a darker chilled margin of *c.* 5 mm, highlighted with an arrow, at the contact with an earlier porphyritic camptonite above (see Fig. 2b).

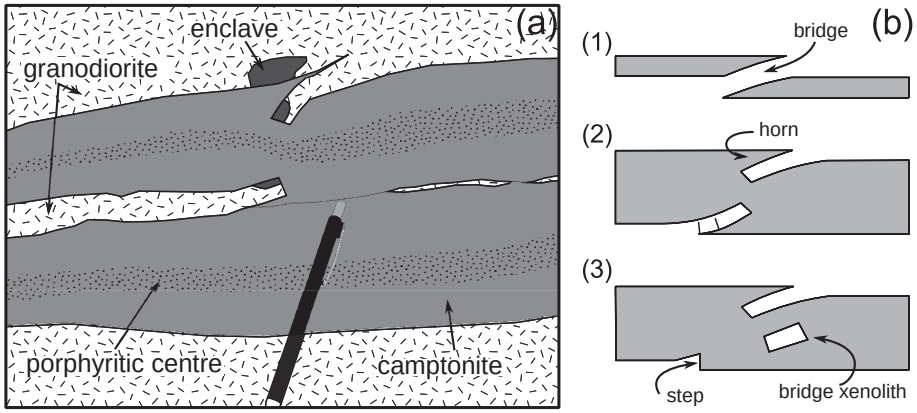

Fig. 4a – Sketch of the contact between the granodiorite wall-rock and two thinner sills of A (Fig. 2a). Pencil length is 15 cm. **b** – Evolutionary model of the lamprophyric magma intrusion along a fracture (Nicholson and Pollard 1985; Cadman et al. 1990). In (1) the initial opening of the fracture leaves a bridge of wall-rock; (2) the wall-rock bridge is broken forming two opposite horns at both dyke contacts; (3) the lower part of the bridge is fragmented forming a xenolith and a step at the contact of the dyke with the wall-rock.

reaching 3–5 mm in size, will be called provisionally macrocrysts, following Rock (1991); their origin will be dealt with below.

In contrast, the part A of the intrusion is formed by several sills (Fig. 2a–b), with a total thickness of about 1 m. In this part A, the intrusive sequence can be deciphered by the existence of chilled margins (Fig. 3b) and septa of granodiorite in between (Fig. 4a). Also, some of these sills side step and form fingers, giving a general irregular shape to this multiple intrusion. In detail, a cross-section of A intrusions shows a lower chilled margin, more altered than the upper chilled one, grading to porphyritic camptonite towards the centre, with macrocrysts of *c.* 5 mm. At few centimetres from the lower contact, this camptonite is intruded by narrow sills, up to 10 cm in thickness, with lower and upper dark chilled margins against the porphyritic host (Fig 3b). Most of these later sills are sub-parallel, but one of them cross-cuts and displaces previous sills (Fig. 2b). In the thinner sills of A, the camptonite is aphyric or with rare macrocrysts concentrating towards the centre.

5. Petrography

The porphyritic varieties of both parts A and B of the intrusion will be described together since they do not show significant differences under the microscope. The mafic minerals form macrocrysts and microliths in the groundmass. Both types are mainly of amphibole, but there is also clinopyroxene. The groundmass shows hypidiomorphic and locally intergranular or intersertal texture. Amygdales, filled with carbonates or less frequently with zeolites, are also present. Both types of amygdales can be observed in the same sample, but the two types of minerals do not co-exist.

The *clinopyroxene* macrocrysts and crystals in the groundmass are colourless under the microscope, subhedral, and partially or completely pseudomorphosed by green chlorite, leaving only clinopyroxene relics (Fig. 5a). These can show a complex oscillatory zoning.

The *amphibole* macrocrysts often consist of either subhedral or rounded brown cores, with narrow subhedral and darker rims (Fig. 5b), similar in colour to that of the

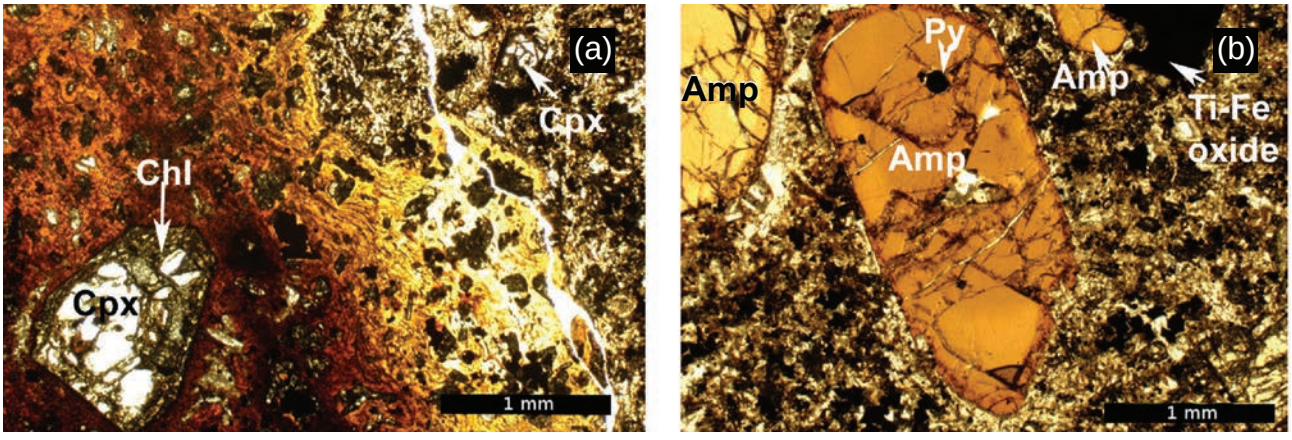

Fig. 5a – Macrocrysts of clinopyroxene (partially transformed into chlorite) in the hypocrystalline fluidal groundmass of the chilled margin from a thinner sill. This sill intrudes an earlier porphyritic camptonite on the right. **b** – Amphibole macrocrysts with subhedral cores overgrown by darker amphibole rims. A phenocryst of ulvöspinel (Ti–Fe oxide) and a pyrite inclusion are also shown. Mineral abbreviations after Whitney and Evans (2010).

Tab. 1 Representative analyses of clinopyroxene

Sample	12SE-3D	12SE-3D	12SE-3D	12SE-3D	12SE-11	12SE-11	12SE-11	12SE-11	12SE-11
Oxides (wt. %)	Macro. C	Macro. C	Groundmass	Groundmass	Macro. C	Macro. M	Macro. R	Groundmass	Groundmass
SiO_2	44.50	46.03	46.90	46.78	45.96	45.14	46.18	43.92	45.29
TiO_2	3.32	2.13	2.46	2.20	2.31	2.61	2.39	3.45	2.37
Al_2O_3	7.91	6.84	5.32	5.35	7.29	8.08	7.07	8.52	7.44
Cr_2O_3	0.00	0.01	0.02	0.01	0.03	0.04	0.02	0.02	0.02
Fe_2O_3(c)	6.84	6.20	5.73	4.87	5.53	6.40	5.95	6.36	6.94
FeO(c)	1.47	3.20	2.42	3.49	3.36	2.87	2.41	1.92	2.75
MnO	0.18	0.18	0.22	0.20	0.17	0.14	0.16	0.17	0.19
MgO	12.56	12.00	14.03	13.69	12.08	11.99	12.68	11.96	11.58
CaO	23.11	22.24	22.79	22.08	22.39	22.62	22.82	23.28	22.39
Na_2O	0.55	0.80	0.31	0.31	0.71	0.64	0.64	0.51	0.85
K_2O	0.00	0.00	0.00	0.04	0.00	0.00	0.00	0.00	0.03
Total	100.45	99.64	100.20	99.01	99.83	100.54	100.31	100.11	99.85
a.p.f.u. based on 6 O, Fe^{3+} estimates after Droop (1987)									
Si	1.657	1.730	1.745	1.762	1.721	1.682	1.718	1.644	1.701
Ti	0.093	0.060	0.069	0.062	0.065	0.073	0.067	0.097	0.067
Al^{IV}	0.343	0.270	0.233	0.237	0.279	0.318	0.282	0.356	0.299
Al^{VI}	0.005	0.032	0.000	0.000	0.043	0.037	0.028	0.020	0.031
Cr	0.000	0.000	0.001	0.000	0.001	0.001	0.001	0.000	0.001
Fe^{3+}	0.192	0.175	0.161	0.138	0.156	0.180	0.166	0.179	0.196
Fe^{2+}	0.046	0.100	0.075	0.110	0.105	0.089	0.075	0.060	0.086
Mn	0.006	0.006	0.007	0.006	0.005	0.004	0.005	0.005	0.006
Mg	0.697	0.672	0.778	0.769	0.674	0.666	0.703	0.667	0.648
Ca	0.922	0.895	0.909	0.891	0.899	0.903	0.910	0.934	0.901
Na	0.040	0.058	0.022	0.022	0.052	0.046	0.046	0.037	0.062
K	0.000	0.000	0.000	0.002	0.000	0.000	0.000	0.000	0.001
mg#	74.1	70.5	76.2	75.2	71.7	70.9	74.1	73.2	69.2
Al^{iV}/Al^{Vi}	0.01	0.12	0.00	0.00	0.15	0.12	0.10	0.06	0.10

Macro.: macrocrystal, C: core, M: medium, R: rim, (c): estimate

amphibole microliths. Resorption of the macrocryst rims is also observed.

Feldspars are only found in the groundmass as microliths or anhedral crystals. Plagioclase is dominant, but alkali feldspars are also present. The distribution of these minerals in the groundmass is heterogeneous, forming spherical or sub-spherical segregations, several millimetres to centimetres across (typical of lamprophyric rocks; Rock 1991), which are also distinguished by the slightly larger size of their microliths. These leucocratic segregations differ from the typical ocelli in lamprophyres, because they grade towards the groundmass, instead of containing crystals of mafic minerals aligned tangentially to their boundaries (Rock 1991; Scarrow et al. 2011). Typical ocelli have not been observed so far in the studied rocks.

Accessory phases are mostly acicular apatite and subhedral Ti–Fe oxide. There are also pyrite, chalcopyrite and pyrrhotite. Secondary chlorite is formed after clinopyroxene, but it also appears in the groundmass. This is also the case of carbonates, which can be also found in the leucocratic segregations, along with sericite, and filling amygdales. Zeolites are rare filling amygdales.

The camptonite at the chilled margins is hypocrystalline, with rare crystals of both clinopyroxene and amphibole in a yellow–dark brown groundmass, with abundant palagonite. A fluidal texture at the contacts between the thinner sills and the central porphyritic camptonite A is observed (Fig. 5a).

6. Mineral chemistry

Clinopyroxene was analysed in two samples (Tab. 1): 12SE-11 from the upper chilled margin of the sill B and 12SE-3D from one of the A thinner sills. In both samples, macrocrysts and crystals in the groundmass were considered. Compositions are of aluminian diopside to augite (Morimoto et al. 1988), with mg number [mg# = 100×Mg/(Mg + Fe_T + Mn), in atoms per formula unit, a.p.f.u.] = 68.2–77.3 and variable Al_2O_3 (4.82–8.52 wt. %) and TiO_2 (2.13–3.45 wt. %) concentrations. The compositions of both types of crystals overlap in sample 12SE-11 (Fig. 6a–c), but in sample 12SE-3D, crystals in the groundmass have higher Si and lower Al abundances than macrocrysts of similar mg# and Ti. A profile from the core towards the rim of one macrocryst shows a com-

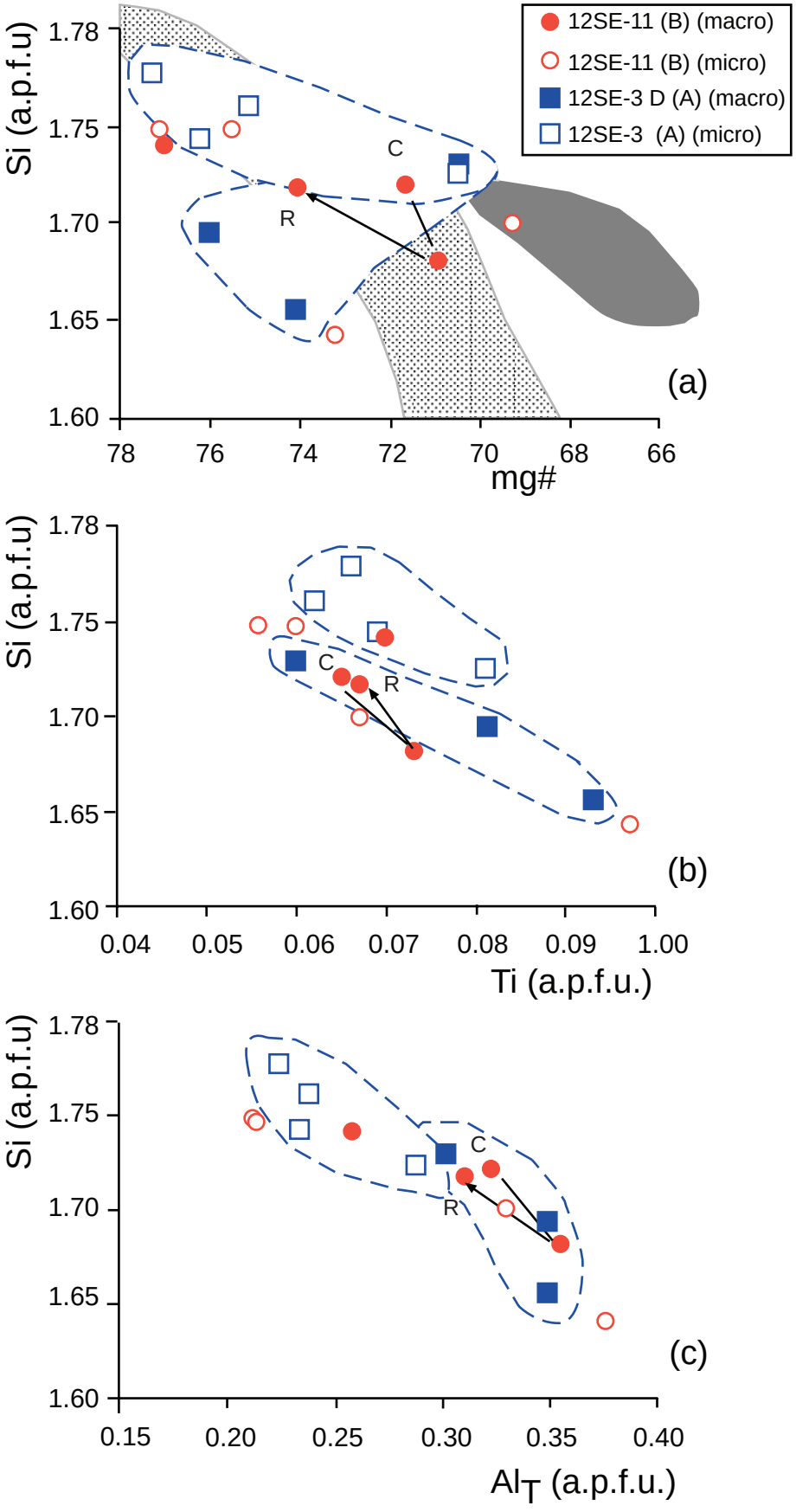

positional trend with inflexions, reflecting its oscillatory zoning. However, the general compositional trend shows roughly positive correlation between Si and mg# (Fig. 6a) and better negative correlation of Si with Ti and Al (Fig. 6b–c).

Amphibole was analysed in four samples (Tab. 2): three from the part A of the intrusion: two from thinner sills (12SE-1 and 12SE-3D) and one from the central porphyritic camptonite (12SE-4); the other sample (12SE-11) is from the upper chilled margin of sill B. Macrocrysts and microliths in the groundmass have kaersutite compositions (Leake et al. 1997), with mg# = 65.9–71.9; the TiO_2 and Al_2O_3 abundances range from 5.02 to 7.33 wt. % and from 13.23 to 17.72 wt. %, respectively. Both Si and mg# tend to decrease from macrocrysts to microliths of the same sample (Fig. 7a, Tab. 3). This compositional variation is also observed from core to rim of macrocrysts (Tab. 3). It is also noticed that the mg# range of amphibole is lower than that of clinopyroxene. The general compositional trend also shows a rough positive correlation between Si and mg# (Fig. 7a).

Fig. 6 Composition of clinopyroxene macrocrysts (macro) and groundmass crystals (micro); A and B stand for the location of samples in the intrusion (see Fig. 2). **a** – Si in atoms per formula unit (a.p.f.u.) vs. mg#; dark grey area is the compositional range for antecryst cores in the nearby camptonite (Ubide et al. 2012), light grey area the compositional range for all antecryst rims, microphenocryst cores and rims of clinopyroxene by the same authors. **b** – Si vs. Ti (a.p.f.u.). **c** – Si vs. Al total (a.p.f.u.). Dashed-line fields highlight clinopyroxene from a thinner sill of part A. C and R stand for core and rim, respectively.

Tab. 2 Representative analyses of amphibole

Sample	12SE-4	12SE-4	12SE-4	12SE-1	12SE-1	12SE-3D	12SE-3D	12SE-11	12SE-11	12SE-11
Oxides (wt. %)	Macro. C	Macro. R	Micro.	Macro. C	Macro. R	Macro. C	Macro. R	Macro.C	Macro. R	Micro.
SiO_2	38.66	38.37	37.28	38.36	38.19	38.90	38.06	38.29	37.28	36.85
TiO_2	4.85	6.35	6.29	5.33	5.28	4.90	6.40	5.06	6.60	7.03
Al_2O_3	14.26	14.28	14.28	13.93	13.94	14.04	13.23	14.04	13.81	14.34
Cr_2O_3	0.09	0.07	0.01	0.02	0.03	0.07	0.00	0.09	0.03	0.01
Fe_2O_3(c)	1.93	0.00	0.00	0.60	0.87	0.64	0.00	0.88	0.00	0.00
FeO(c)	7.88	10.14	11.09	9.71	9.63	8.93	10.23	9.04	10.06	9.92
MnO	0.07	0.11	0.21	0.18	0.09	0.05	0.13	0.10	0.06	0.16
MgO	13.64	12.71	12.33	13.04	13.10	13.65	13.10	13.65	12.97	12.97
CaO	12.03	12.69	12.46	12.08	12.00	12.14	12.69	12.22	12.68	12.55
Na_2O	1.92	2.09	2.45	2.15	2.29	2.01	2.33	2.27	2.35	2.20
K_2O	1.82	1.35	1.22	1.65	1.67	1.95	1.21	1.85	1.26	1.33
F	0.07	0.00	0.51	0.44	0.65	0.51	0.44	0.00	0.00	0.30
Cl	0.03	0.00	0.02	0.02	0.03	0.01	0.02	0.02	0.05	0.03
O=F	0.03	0.00	0.21	0.18	0.27	0.22	0.19	0.00	0.00	0.12
O=Cl	0.01	0.00	0.00	0.00	0.01	0.00	0.00	0.00	0.01	0.01
Total	97.21	98.16	97.94	97.33	97.49	97.58	97.65	97.51	97.14	97.56
a.p.f.u. based on 23 O, Fe^{3+} estimates after Robinson et al. (1982), assuming ∑ cations = 13 except for Ca, Na and K										
Si	5.737	5.671	5.582	5.735	5.712	5.778	5.686	5.697	5.589	5.510
Ti	0.541	0.706	0.708	0.599	0.593	0.547	0.719	0.566	0.745	0.790
Al ^{IV}	2.263	2.329	2.418	2.265	2.288	2.222	2.314	2.303	2.411	2.490
Al ^{VI}	0.230	0.158	0.101	0.189	0.169	0.236	0.016	0.159	0.030	0.036
Cr	0.011	0.008	0.001	0.002	0.004	0.008	0.000	0.011	0.003	0.002
Fe^{3+}	0.215	0.000	0.000	0.067	0.098	0.072	0.000	0.098	0.000	0.000
Fe^{2+}	0.978	1.253	1.388	1.214	1.205	1.109	1.279	1.125	1.262	1.240
Mn	0.008	0.014	0.027	0.023	0.012	0.006	0.017	0.012	0.007	0.021
Mg	3.016	2.800	2.751	2.906	2.919	3.022	2.917	3.028	2.898	2.890
Ca	1.914	2.010	1.999	1.936	1.923	1.932	2.031	1.949	2.037	2.011
Na	0.552	0.598	0.713	0.623	0.664	0.579	0.675	0.655	0.684	0.639
K	0.345	0.254	0.233	0.314	0.319	0.369	0.230	0.351	0.242	0.254
F	0.034	0.000	0.241	0.207	0.308	0.240	0.208	0.000	0.000	0.140
Cl	0.007	0.001	0.004	0.005	0.008	0.002	0.005	0.004	0.012	0.007
mg#	71.5	68.8	66.0	69.0	68.9	71.8	69.2	71.0	69.5	69.6
k#	38.5	29.8	24.6	33.5	32.5	38.9	25.4	34.9	26.1	28.4

Macro.: macrocrystal, Micro.: microcrystal, C: core, R: rim, (c): estimate

A positive correlation also exists between Si and k number [k# = 100×K/(K + Na), in a.p.f.u.] for macrocrysts. Kaersutite microliths show the lowest k# (Fig. 7b). Finally, as in clinopyroxene, Si is negatively correlated with Ti and Al (Fig. 7c–d), although the correlation between Si and Al is worse.

Feldspars were analysed in four samples (Tab. 3): two from A intrusions, including the central porphyritic camptonite (12SE-4) and one thinner sill (12SE-3D), and two from the sill B (12SE-11 and 12SE-13). In all cases, plagioclase is dominant, in accordance with the definition of camptonite (Le Maitre et al. 2002), with compositions from labradorite to potassic oligoclase (Smith and Brown 1988) but there is also alkali feldspar ranging from calcic anorthoclase to potassic sanidine compositions (Fig. 8). The latter one is only found in the leucocratic segregations. In sill B, plagioclase has higher orthoclase component in solid solution.

Among the accessory minerals, most Ti–Fe oxides show compositions of titanomagnetite–ulvöspinel, with 15–19 wt. % TiO_2 (Tab. 4). They occasionally enclose rounded cores of ilmenite. Carbonate in sample 12SE-3D is calcite (96.1 mol. %), with low content of siderite (0.9 mol.%), magnesite (2.6 mol. %) and eitelite (0.4 mol.%), whereas in sample 12SE-11 from sill B, it is dolomite (Cal: 56.3, Mgs: 33.8, Sd: 9.8, eitelite: 0.1) and siderite (Sd: 59.5, Mgs: 26.3, Cal: 13.5, eitelite: 0.4, witherite: 0.1), all components in mol. %.

7. Whole-rock geochemistry

The location of the analysed samples (Tab. 5) is shown in Fig. 2. Four samples correspond to the part A of the intrusion and three to sill B. The loss on ignition (LOI) can reach 12 wt. % because of the abundance of carbonates and hydrated minerals in these rocks.

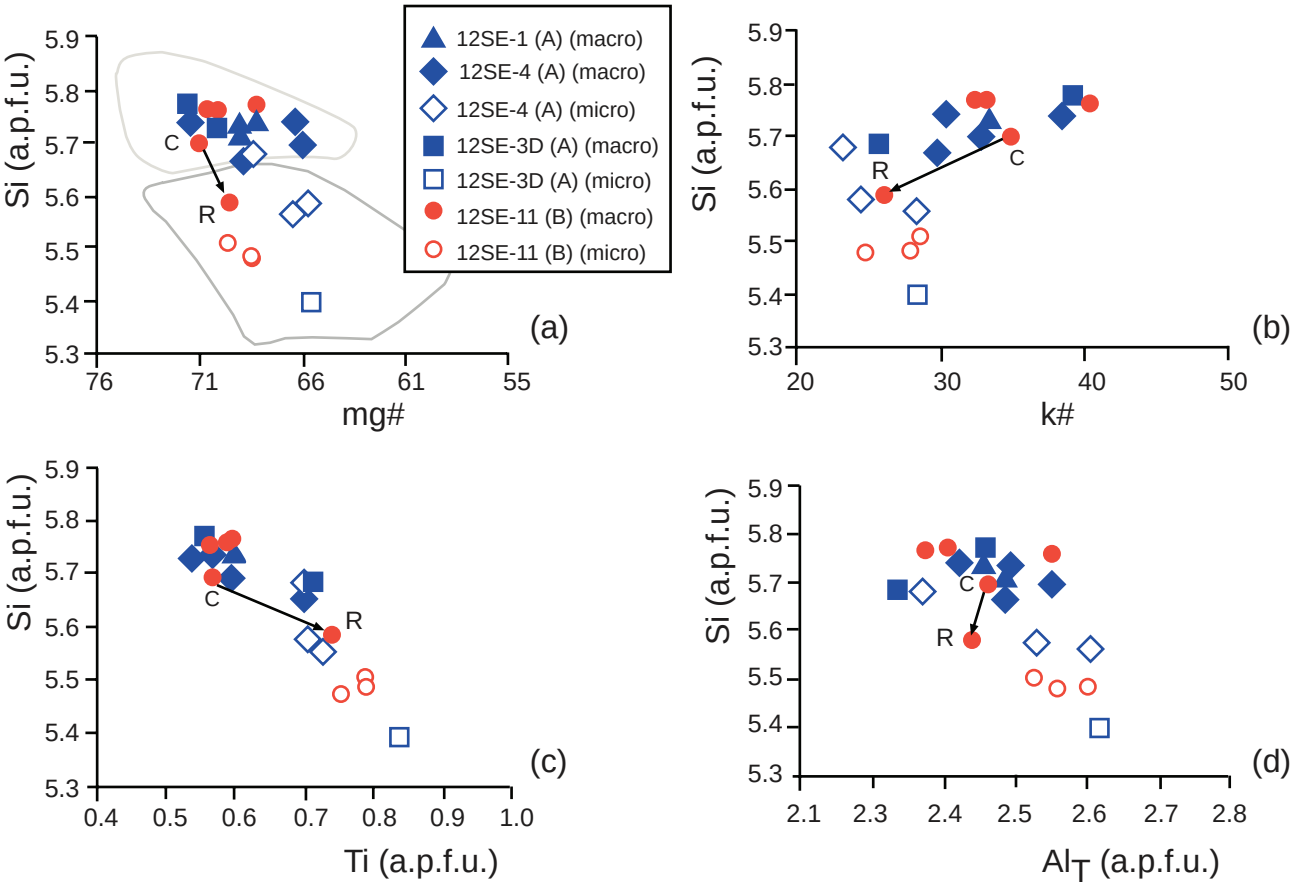

Fig. 7 Composition of amphibole macrocrysts and microliths (a.p.f.u.). **a –** Si vs. mg# plot; dark grey area is the compositional range for amphibole antecryst and microphenocryst cores (Ubide et al. 2012), the light grey area is the field for all antecrysts, microphenocryst rims and microliths of amphibole in the groundmass by the same authors. **b** – Si vs. k# plot. **c** – Si vs. Ti plot. **d** – Si vs. Al total plot. The arrows indicate the compositional variation from core (C) to rim (R) of a single macrocrystal.

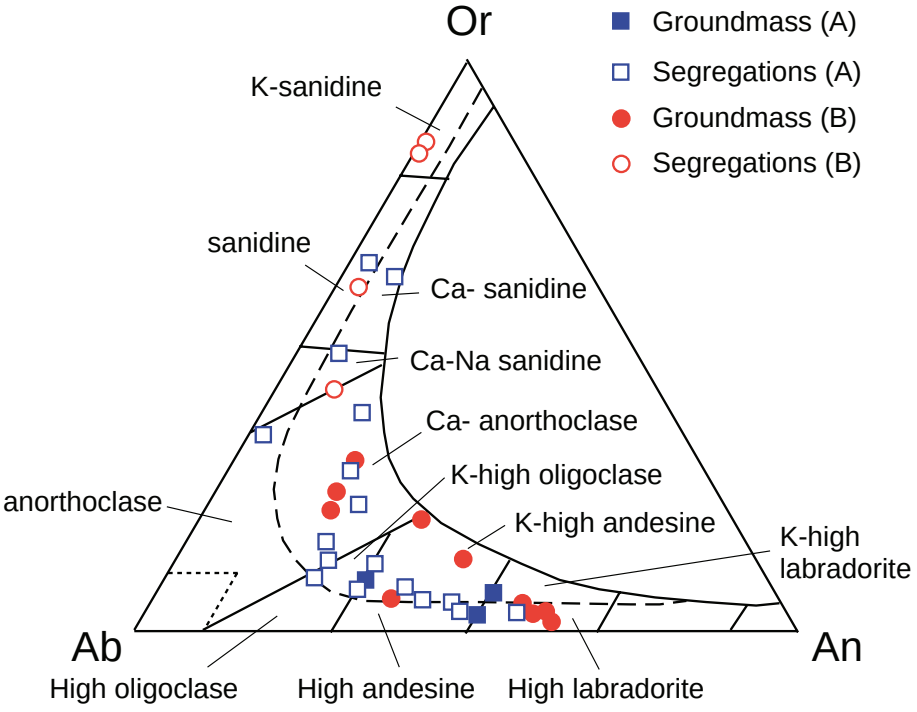

All samples in Tab. 5 are ultrabasic, equivalent to tephrites in the total alkali vs. SiO_2 diagram (Le Maitre et al. 2002, not shown). On the anhydrous basis, the SiO_2 ranges from 41 to 45 wt. % and the total alkali range is from 5.6 to 6.2 wt. %. Samples from sill B are slightly potassic ($K_2O > Na_2O$ in wt. %), whereas those from sill A are sodi–potassic ($Na_2O - 4 < K_2O < Na_2O$ in wt. %) (Le Bas et al. 1986). This is reflected in the higher amount of normative leucite of the camptonites from

Fig. 8 Compositional variation and nomenclature of feldspars from the groundmass and the segregations of sills B and A. The nomenclature is after Smith and Brown (1988) for disordered ternary feldspars.

Tab. 3 Representative analyses of feldspars

Sample	13SE-04				12SE-3D			12SE-11					12SE-13	
Oxides (wt. %)	1	2	3	4	1	2	3	1	2	3	4	5	1	2
SiO_2	50.48	52.35	60.64	61.02	53.62	58.22	62.59	60.22	52.47	61.42	58.92	63.99	64.22	65.76
TiO_2	0.14	0.20	0.31	0.61	0.18	0.19	0.02	0.23	0.17	0.17	1.22	0.05	0.13	0.11
Al_2O_3	30.03	28.49	21.97	20.26	27.60	25.42	20.50	23.57	28.79	23.22	21.38	18.38	19.25	20.23
Fe_2O_3	0.87	0.96	0.67	1.72	0.87	0.82	0.15	0.50	0.74	0.39	0.72	0.44	0.42	0.31
MgO	0.09	0.12	0.03	0.30	0.05	0.05	0.02	0.02	0.09	0.00	0.02	0.00	0.03	0.02
CaO	13.31	11.35	3.74	1.82	10.26	7.26	0.86	4.92	11.46	4.71	3.27	0.13	0.51	0.45
BaO	0.00	0.14	0.93	0.00	0.01	0.19	0.10	0.00	0.19	0.00	0.03	0.10	0.00	0.00
Na_2O	4.26	4.42	6.90	5.55	5.35	6.77	4.87	8.16	4.72	7.42	5.87	1.61	3.78	7.42
K_2O	0.41	0.83	4.40	7.42	0.63	1.04	12.46	1.65	0.52	2.24	7.36	14.56	11.61	6.24
Total	99.59	98.87	99.60	98.70	98.58	99.96	101.58	99.26	99.14	99.59	98.80	99.27	99.94	100.54
a.p.f.u. based on 8 O														
Si	2.321	2.412	2.768	2.818	2.466	2.620	2.856	2.718	2.408	2.756	2.737	2.975	2.939	2.931
Ti	0.005	0.007	0.011	0.021	0.006	0.006	0.001	0.008	0.006	0.006	0.043	0.002	0.005	0.004
Al	1.627	1.547	1.182	1.103	1.496	1.348	1.103	1.254	1.557	1.228	1.171	1.007	1.038	1.063
Fe^{3+}	0.030	0.033	0.023	0.060	0.030	0.028	0.005	0.017	0.026	0.013	0.025	0.016	0.015	0.010
Mg	0.006	0.009	0.002	0.021	0.004	0.004	0.001	0.001	0.006	0.000	0.002	0.000	0.002	0.001
Ca	0.655	0.560	0.183	0.090	0.506	0.350	0.042	0.238	0.563	0.227	0.163	0.006	0.025	0.022
Ba	0.000	0.003	0.017	0.000	0.000	0.003	0.002	0.000	0.003	0.000	0.001	0.002	0.000	0.000
Na	0.380	0.395	0.611	0.497	0.477	0.591	0.431	0.714	0.420	0.646	0.529	0.145	0.335	0.641
K	0.024	0.049	0.256	0.437	0.037	0.059	0.726	0.095	0.030	0.128	0.436	0.864	0.678	0.355
Ab %	35.9	39.3	57.3	48.5	46.8	58.8	35.9	68.2	41.3	64.5	46.9	14.3	32.3	63.0
An %	61.9	55.7	17.2	8.8	49.5	34.9	3.5	22.7	55.4	22.6	14.4	0.6	2.4	2.1
Or %	2.3	4.8	24.0	42.7	3.6	5.9	60.5	9.1	3.0	12.8	38.7	84.9	65.3	34.9

Feldspar components in mol. %

sill B. Other differences are observed in the co-variation diagrams (Fig. 9): camptonites from sill B have the lowest SiO_2 and the highest CaO abundances (Fig. 9a); the slight increase in SiO_2 from bottom to top of the sill B

Tab. 4. Representative analyses of Fe–Ti oxides

Sample	12SE-3D	12SE-4	12SE-1	12SE-3D	12SE-11	12SE-13
Oxides (wt. %)	Ilm	Timag-Usp	Timag-Usp	Timag-Usp	Timag-Usp	Timag-Usp
SiO_2	0.00	0.25	0.38	0.21	0.86	0.83
TiO_2	38.95	15.76	16.69	18.64	18.73	16.31
Al_2O_3	0.90	7.08	7.18	5.75	6.88	7.71
Cr_2O_3	0.05	0.10	0.05	0.03	0.07	0.05
Fe_2O_3(c)	28.07	30.97	27.31	25.70	22.03	26.63
FeO(c)	27.49	33.95	35.83	37.78	39.36	35.75
MnO	0.33	0.46	0.52	0.57	0.49	0.47
MgO	4.03	7.58	6.70	6.34	5.99	7.03
Total	99.83	96.16	94.67	95.02	94.41	94.79
a.p.f.u. based on 3 O for ilmenite and 4 O for Ti-magnetite–ulvöspinel, Fe^{3+} estimates based on charge balance after Droop (1987)						
Si	0.000	0.009	0.014	0.008	0.031	0.030
Ti	0.725	0.424	0.457	0.514	0.516	0.443
Al	0.026	0.298	0.308	0.248	0.297	0.328
Cr	0.001	0.003	0.002	0.001	0.002	0.001
Fe^{3+}	0.523	0.833	0.748	0.709	0.607	0.724
Fe^{2+}	0.569	1.015	1.091	1.157	1.205	1.080
Mn^{2+}	0.007	0.014	0.016	0.018	0.015	0.014
Mg	0.149	0.404	0.364	0.346	0.327	0.379
Ilm %	57.7					
Gk %	15.1					
Pph %	0.7					
Hem %	26.5					

Ilmenite components in mol. %. Mineral abbreviations of Whitney and Evans (2010), other symbols as in Tab. 1

Tab. 5 Major- and trace-element analyses with CIPW norms of the studied camptonites.

Oxides (wt. %)	12SE-2	12SE-4	12SE-1	12SE-3D	12SE-11	12SE-12B	12SE-13	Precision % (1σ)
SiO_2	39.80	41.20	38.20	40.20	36.80	36.60	36.30	*5*
TiO_2	3.79	3.70	3.55	3.89	3.82	3.64	3.59	*9*
Al_2O_3	14.05	14.60	13.70	13.90	14.00	14.10	14.15	*5*
Fe_2O_3T	14.15	13.55	13.40	14.00	12.85	12.30	11.40	*5*
MnO	0.18	0.15	0.20	0.19	0.21	0.22	0.21	*29*
MgO	3.88	3.38	3.26	3.96	3.39	3.19	2.43	*6*
CaO	10.15	9.47	11.70	10.40	11.95	12.50	12.85	*5*
Na_2O	2.74	2.87	3.02	3.05	2.34	2.46	2.41	*6*
K_2O	2.52	2.72	2.53	2.47	2.63	2.69	2.78	*5*
P_2O_5	0.69	0.75	0.70	0.61	0.64	0.66	0.66	*33*
LOI	8.85	8.17	10.80	8.48	9.82	10.55	12.05	*5*
Total	100.80	100.56	101.06	101.15	98.45	98.91	98.83	
Mg#	35.2	33.1	32.5	35.9	34.3	33.9	29.7	
K#	37.7	38.4	35.5	34.8	42.5	41.8	43.1	
CIPW norm (wt. %)								
or	16.2	17.4	14.9	15.7	7.7	4.0	7.6	
ab	8.1	13.1	0.0	7.3	0.0	0.0	0.0	
an	20.2	20.5	18.1	18.3	22.5	22.0	22.6	
ne	9.2	7.1	15.3	11.3	12.1	12.7	12.7	
lc	0.0	0.0	1.3	0.0	7.7	10.9	8.9	
di	24.6	20.9	32.9	27.4	32.9	32.0	26.2	
wo	0.0	0.0	0.6	0.0	0.0	2.0	6.1	
ol	4.2	3.8	0.0	2.9	0.3	0.0	0.0	
mt	7.9	7.8	7.6	7.9	7.0	6.8	6.4	
il	7.8	7.6	7.5	8.0	8.2	7.8	7.8	
hap	1.8	1.9	1.8	1.6	1.7	1.8	1.8	
Total	100.0	100.0	100.0	100.2	100.0	100.0	100.0	
Trace elements (ppm)								
Sc	19	17	17	19	20	18	17	*29*
V	432	398	383	426	445	409	359	*58*
Cr	100	30	10	20	20	20	10	*50*
Co	34	40	37	37	37	35	33	*30*
Ni	32	18	14	14	16	17	12	*10*
Cu	37	40	42	45	43	39	40	*10*
Zn	112	93	115	109	115	106	124	*10*
Ga	25.9	25.6	24.4	25.4	24.7	23.8	23.7	*10*
Ba	645	766	536	609	545	556	492	*9*
Rb	93.7	98.6	95.7	95.2	118	119	140	*11*
Sr	954	1010	889	896	898	922	869	*10*
Y	26.2	27.6	30.8	30.7	26.3	26.3	28.6	*12*
Zr	270	290	270	280	280	280	270	*21*
Nb	66.0	71.9	67.8	66.6	64.3	65.7	66.3	*11*
Mo	1	1	1	1	1	1	1	*13*
Hf	7.0	6.9	6.6	6.8	7.2	7.2	7.0	*12*
La	49.5	52.8	50.8	49	50.6	51.8	53.4	*11*
Ce	105	112	110.5	110	101	103.5	105	*11*
Pr	13.10	14.20	14.25	14.40	13.35	13.55	13.80	*10*
Nd	53.6	57.5	59.5	61.3	51.8	52.2	52.6	*10*
Sm	9.72	10.45	11.40	11.80	9.94	10.00	10.10	*10*
Eu	2.60	2.82	3.05	3.22	2.86	2.90	2.85	*14*
Gd	7.99	8.66	9.55	9.62	8.23	8.00	8.36	*10*
Tb	1.04	1.12	1.19	1.24	1.05	1.04	1.09	*12*
Dy	5.33	5.74	6.24	6.28	5.44	5.43	5.76	*11*
Ho	0.97	1.06	1.14	1.15	0.97	0.97	1.02	*12*
Er	2.47	2.6	2.82	2.68	2.53	2.54	2.68	*11*
Tm	0.34	0.35	0.35	0.35	0.32	0.32	0.33	*14*
Yb	2.03	2.14	2.13	2.14	1.91	1.92	1.99	*11*
Lu	0.29	0.29	0.3	0.28	0.27	0.28	0.29	*13*
Ta	4.3	4.6	4.3	4.2	3.9	4.0	4.1	*16*
Pb	10	10	9	9	3	3	3	*11*
Th	4.85	5.36	4.95	4.85	4.71	4.87	4.91	*10*
U	1.62	1.66	1.64	1.42	1.38	1.41	1.45	*10*
$(La/Yb)_N$	17	17	16	16	18	18	18	
$(Gd/Yb)_N$	3.2	3.3	3.6	3.6	3.5	3.4	3.4	
V/Cr	4.3	13	38	21	22	20	36	
Nb/Pb	6.6	7.2	7.5	7.4	21	22	22	
La/Th	10	10	10	10	11	11	11	
Ba/Th	133	143	108	126	116	114	100	
Th/U	3.0	3.2	3.0	3.4	3.4	3.5	3.4	

CIPW norms estimated with the IUGSTAS software (Le Maitre et al. 2002); $FeO/(FeO+Fe_2O_3)$ calculated after Le Maitre (1976) for volcanic rocks. REE ratios normalized to chondritic values of McDonough and Sun (1995). Location of samples in Fig. 2

(36.3–36.8 wt. %, Tab. 5) is considered insignificant. Camptonites from part A of the intrusion display scatter. Only the CaO vs. SiO_2 diagram shows a good linear correlation.

Other camptonites from the same zone (Velde and Tournon 1970; Enrique 2009; Ubide et al. 2012) cropping out further south are also plotted (Fig. 9). It is noteworthy that the Mg number [Mg# = 100×MgO/(MgO + FeO_T), mol. %] of the studied camptonites is lower than that of similar rocks nearby, while the K number [K# = 100×K_2O/(K_2O + Na_2O), mol. %] reaches the highest values in camptonites from sill B. Also, the best general correlation is observed in the CaO vs. SiO_2 diagram (Fig. 9a), which illustrates that the camptonites from Platja Fonda show lower SiO_2 and higher CaO contents than similar rocks nearby.

The binary plots of trace elements vs. SiO_2 (Fig. 10) are also mostly scattered. Only Ba and the Rb/Sr ratio show a better correlation with SiO_2, the former positive (Fig. 10g) and the latter negative (Fig. 10h), from the potassic towards the sodi–potassic camptonites. All samples have V/Cr and Nb/Pb ratios within, or near, the ranges for alkaline lamprophyres (Rock 1991), but camptonites from sill B also differ by higher Nb/Pb ratios: 17–18 for the potassic and 5–7 for the sodi–potassic types.

In the Primitive Mantle (McDonough and Sun 1995) normalized multielement diagrams, all samples display generally similar patterns. However, the camptonites from B show a small negative, and camptonites from A slightly positive anomaly of Pb (Fig. 11). Such patterns with high concentrations of large-ion lithophile elements (LILE), Nb–Ta and REE are characteristic of mafic alkaline melts. Light REE (LREE) are similarly fractionated with respect to heavy REE (HREE) in all samples (La/Yb_N = 16–18). The HREE are also mutually fractionated (Gd/Yb_N = 3–4).

Generally, the newly obtained analyses match the patterns of other camptonites in this area (Ubide et al.

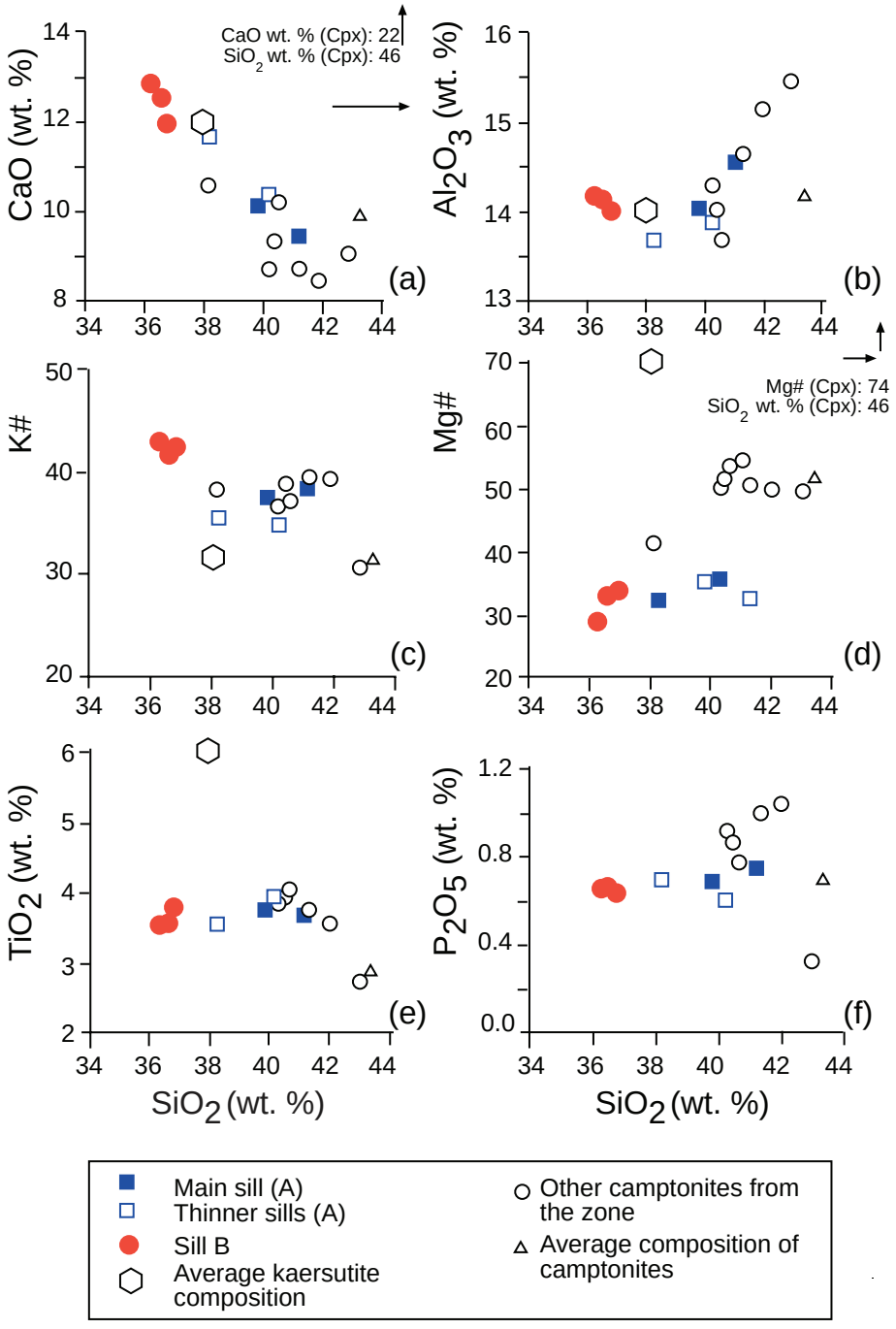

Fig. 9a–f Whole-rock co-variation diagrams for selected major-element oxides, K# and Mg# vs. SiO_2 concentration. Data from other camptonites in the Catalan Coastal Ranges are from Velde and Tournon (1970), Enrique (2009) and Ubide et al. (2012). Average composition of camptonites is from Rock (1991). Average compositions of kaersutite amphibole and clinopyroxene are from this study.

2012). The La/Yb_N values are slightly lower than in the Cretaceous lamprophyres from the eastern Pyrenees, while the Gd/Yb_N ratios are similar (La/Yb_N = 24–27, Gd/Yb_N = 3, according to Azambre et al. 1992). Also their multielement diagrams are characterized by small negative anomalies of Th, Zr–Hf and Y.

8. Discussion

8.1. Mechanisms of intrusion

The macrostructures observed in the multiple intrusion of Platja Fonda (Figs 2 and 4a) are best explained as having resulted from injections of the lamprophyric magmas along a pre-existing joint or fracture system (San Miguel Arribas 1952; Martínez-Poza et al. 2012), reactivated during the emplacement. According to the model of Nicholson and Pollard (1985) and Cadman et al. (1990) (Fig. 4b), the magma would have initially taken advantage of a pre-existing fracture to intrude. The opening of this fracture would have generated a bridge of wall-rock, which would later have broken, joining the two sides of the sill, and leaving two opposite horns at both sides of the dyke. Finally, one part of the broken bridge could be fragmented by the magma dynamics, forming a xenolith and one step at the contact with the wall-rock. The upper dyke in the cross-section of Fig. 4a would correspond to the arrested second stage in Fig. 4b. Since a microgranular enclave in the granodiorite was cross-cut, but not horizontally displaced, by one of the thinner sills (Fig. 4a), it is inferred that there was no relative lateral movement along the fracture. Therefore, its dilation must have been orthogonal to the strike.

On the other hand, the existence of long wall-rock septa in between two thinner sills (Fig. 4a) could be explained according to the following model. First, the lamprophyric magma would have intruded along a fracture (Fig. 12a) and solidi-

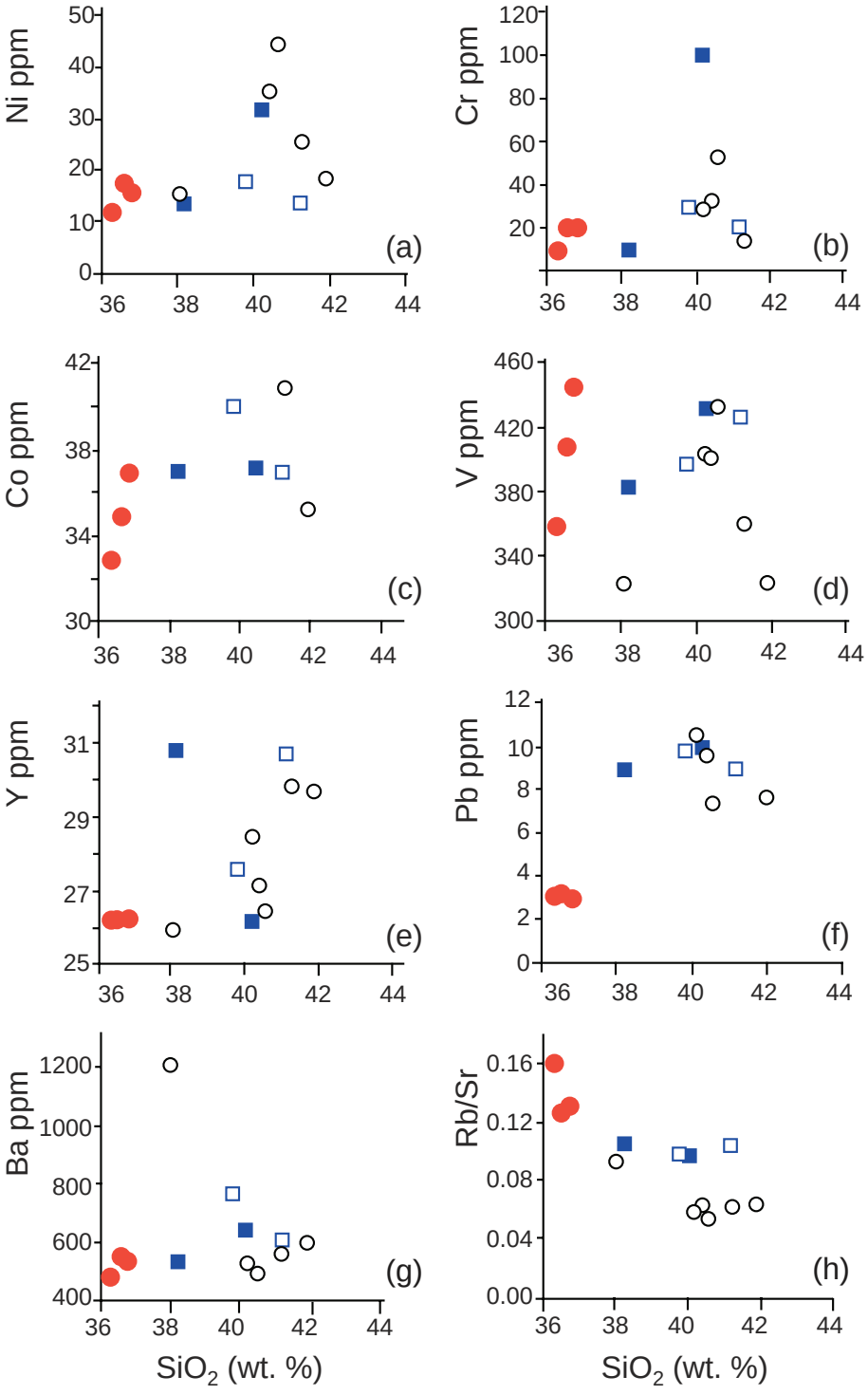

Fig. 10a–h Co-variation diagrams of the whole-rock trace-element contents and Rb/Sr ratio vs. SiO_2 concentration. Symbols as in Fig. 9.

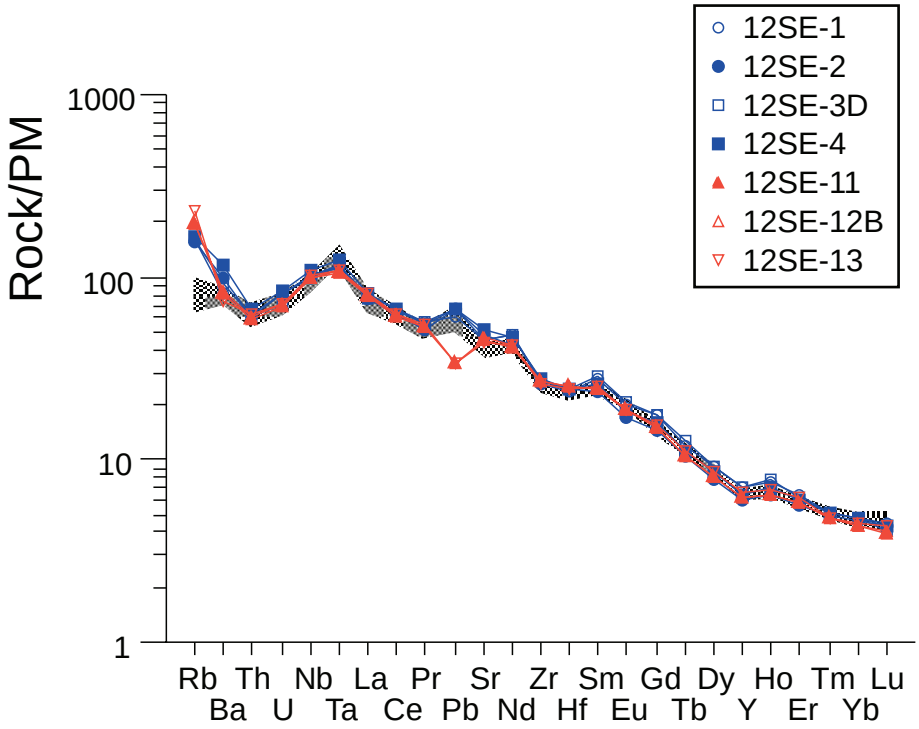

Fig. 11 Multielement diagram with trace-element abundances normalized to the Primitive Mantle (McDonough and Sun 1995). The grey area represents compositions for nearby camptonites (Ubide et al. 2012).

fied. Then, a second intrusion would have occurred taking advantage of the previous dyke contact. However, it would have side-stepped (Fig. 12b), when it had found another weaker zone over the previous fracture, trapping a wall-rock septum between the two sills (Fig. 12c).

Finally, the existence of chilled margins in the thinner sills of part A, at the contact with the central porphyritic camptonite (Fig. 3b), would imply that the latter was already cold when it was intruded by new camptonite magma pulses.

8.2. Macrocryst origin

Clinopyroxene and amphibole macrocrysts from another camptonite dyke nearby were recently interpreted as antecrysts by Ubide et al. (2012), because they show slightly different compositions with respect to crystals in the groundmass (Figs 6a, 7a). According to Jerram and Martin (2008), antecrysts are defined as crystals that have been incorporated into the final magma, but have formed from its progenitor. They may have been originally stored as cumulates at depth, and then recycled through different magma pulses, or could have been reincorporated during the final stages of emplacement. Thus, they are related to the active magmatic system, but not in equilibrium with the melt represented by the groundmass.

In the camptonites studied here, there is no clear evidence of such an origin for the diopside–augite and kaersutite macrocrysts. To begin with the clinopyroxene, only one sample shows a slight compositional difference between macrocrysts and crystals in the groundmass (Fig. 6a). Moreover, most compositions plot outside the compositional range for the clinopyroxene antecrysts of Ubide et al. (2012) (Fig. 6a). Lastly, although zoned crystals indicate that they are not in equilibrium with the surrounding melt, the oscillatory zoning observed in the clinopyroxene macrocrysts could be due to transport-reaction kinetic effects during their local crystallization rather than to their growth from different melts (Shimizu 1990). Alternatively, this zoning could be the result of extrinsic mechanisms, independent of local crystallization (Shore and Fowler 1996). These would have caused physical or chemical changes within the bulk system, such as crystal settling, large-scale convection, recharge and magma mixing in a deeper magma chamber. The fact that the Al^{IV}/Al^{VI} ratio in both macrocrysts and microcrysts of clinopyroxene largely overlaps, together with similar Na abundances in both types of crystals (Tab. 2), suggests that their proportions of tschermakite and jadeite components do not differ. Therefore, their pressure of formation would have not been significantly different (Aoki and Shiba 1973).

In an attempt to estimate this pressure, the barometer by Nimis and Ulmer (1998) and Nimis (1999), based on the unit-cell volume vs. M1 site volume, was used. For such a purpose, it was assumed melt composition comparable to a water-saturated alkali basalt, for which the clinopyroxene begins to crystallize at *c.* 1000 ºC (Yoder and Tilley 1962). Macrocrysts and crystals in the groundmass of the same sample (12SE-11) provide similar results (7 ± 1 kbar). Therefore, in absence of another compositional data, the clinopyroxene macrocrysts in the

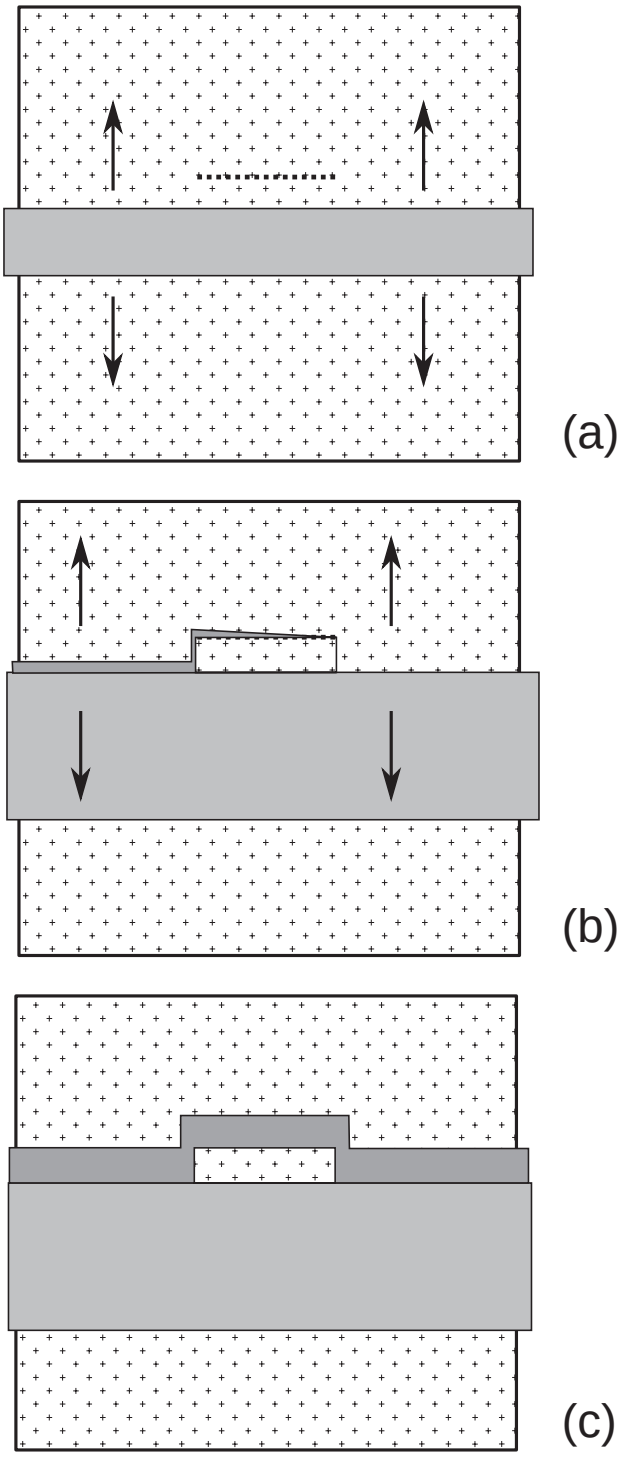

Fig. 12 Model for the formation of narrow angular wall-rock septa between two intrusions of camptonite. **a** – Injection of the camptonite magma along one of the pre-existing fractures and its solidification; **b** – intrusion of the second pulse of magma along the contact between the wall-rock and the previous sill. The second pulse of magma side-steps taking advantage of the weaker zone around the upper fracture. **c** – The wall-rock xenolith becomes trapped between the two sills.

Platja Fonda camptonites could be phenocrysts grown at greater depth during an earlier crystallization of the camptonitic magma. Crystals in the groundmass could have been formed in similar conditions, but ascended without enough time to grow. Otherwise, the compositions of these two types of crystals would have been insensitive to changing pressure during the crystallization.

Regarding kaersutite, the compositions of macrocryst cores are slightly enriched in Si. Also, they have lower Ti and Al abundances and higher mg# and k# than the macrocryst rims and microliths of the same sample (Fig. 7a–c). It is worth noting that the core compositions are comparable to those of the antecryst cores of Ubide et al. (2012) (Fig.7a). Their crystallization at depth from a precursor magma of the camptonites, with higher Mg# and lower SiO_2 activity than the host magma, could explain the rounded shape and sharp contacts with the darker rims (Fig. 5b). These cores would have been partially dissolved during their incorporation in the host magma. However, taking into account that their composition is only slightly different with respect to that of rims and microliths, they could be also interpreted as phenocrysts, but formed at greater depth, since Ti partition coefficient in amphibole decreases with increasing pressure (Adam and Green 1994). In addition, if ilmenite had crystallized simultaneously with kaersutite, the incorporation of Ti in the latter would have decreased. Both earlier kaersutite and ilmenite crystals would have been resorbed later, due to rapid magma ascent or volatile exsolution (Bédard 1988). The thermometer of Otten (1984) provides temperatures for the phenocryst cores very similar in all camptonites (1031 ± 7 °C). Values for the phenocryst rims and microliths are also rather homogeneous (1071 ± 17 °C) and only slightly higher, but they must be considered with caution, because this kaersutite did not co-exist with ilmenite (Otten 1984).

8.3. The lamprophyric magmas

The results of this study indicate that the multiple intrusion of Platja Fonda includes slightly heterogeneous camptonites, ranging from sodi–potassic to potassic. This weak chemical difference could represent pulses either from the same magmatic system, with a variable degree of differentiation, or resulting from differences in the partial melting processes at depth, such as involvement of heterogeneous sources, distinct melting minerals, degree of melting, or changes in the melting conditions. The fact that sample 12SE-1, from a late thinner sill of intrusions A (Fig. 2b), has a low amount of normative leucite (Tab. 5) may indicate a gradual transition between them. It could also imply that the most potassic camptonites would be the last to intrude, although this relationship is to be confirmed. So far, camptonites with potassic

character have not been mentioned in this area. They exist in the Central Iberian Zone of the Iberian Massif (Julivert et al. 1972), although Permian in age (Orejana et al. 2008; Scarrow et al. 2011). The range of ages for the camptonites of the studied area corresponds to Late Cretaceous (69–81 Ma, Solé et al. 2003), more akin to the Middle Cretaceous age of alkaline rocks in the Pyrenees, which also include potassic lamprophyres (sannaites) (Azambre el al. 1992).

Assuming that late or postmagmatic processes did not affect significantly the compositions of these rocks, scatter in most of the binary diagrams (Figs 9–10) precludes a simple link by fractional crystallization between the two camptonite types. The best, negative correlation is displayed by CaO and SiO_2 (Fig. 9a). The potassic camptonites have the lowest SiO_2 and the highest CaO concentrations. This correlation cannot be due to plagioclase fractionation: this mineral does not appear as phenocrysts and no significant negative anomalies of Eu and Sr are observed in multielement diagrams (Fig. 11). Fractionation of clinopyroxene alone must be also excluded because it is too siliceous and does not plot along the trend in Fig. 9a. This leaves kaersutite as the most likely "extract", because it plots within the CaO–SiO_2 trend (Fig. 9a).

Alternatively, this trend may be due to variable proportions of carbonates: slightly higher LOI and CaO concentrations are observed in the potassic camptonites than in the sodi-potassic ones (Tab. 5). However, since carbonates capture more Sr and Ba than Rb, the Rb/Sr ratio and the Ba concentrations would be lower and higher, respectively, in the former than in the latter, which it is not the case (Fig. 10g, h). On the other hand, a kaersutite-driven fractionation could explain the Al_2O_3–SiO_2, TiO_2–SiO_2 and K#–SiO_2 variations (Figs 9b, c, e) among the sodi-potassic camptonites. However, this idea does not fit the trends observed in other variation diagrams (e.g., Mg# vs. SiO_2; Fig. 9d). It is worth noting that increasing of both Mg# and SiO_2 from the Platja Fonda camptonites to those situated further south (Fig. 9d), matches the compositional variation between the microliths and the cores of kaersutite phenocrysts (Fig. 7a). This fact could indicate a higher accumulation of kaersutite and clinopyroxene phenocrysts (or antecrysts of Ubide et al. 2012) in the southern outcrops. However, this hypothesis is in contradiction with the general negative correlation between K# and SiO_2 abundances (Fig. 9c) as the cores of kaersutite phenocrysts are more potassic than the rims and microliths (Fig. 7b). It is also against the role of kaersutite in the other variation diagrams (Fig. 9). Nevertheless, this regional trend in Fig. 9d could be also explained by fractionation of Ti–Fe oxides.

On the other hand, the camptonites from Platja Fonda show lower Mg# values (36–29) and lower abundances of Cr and Ni (Tab. 5) than primary mantle melts (Mg#: 65–80, Rock 1991). Nevertheless, the observed low SiO_2 abundances exclude significant crustal contamination. Therefore, the studied camptonites must represent: (1) evolved mantle melts resulting from a certain degree of differentiation at depth or (2) primary partial melts of a metasomatized mantle. This would apply to all samples from the chilled margins (12SE-11 and 12SE-13 in Tab. 5), the aphyric camptonites from the A thinner sills (12SE-1 and 12SE-3D) and to the porphyritic facies (SE12-2 and SE12-4): the compositional difference between aphyric camptonites and the porphyritic ones is minimal. Therefore, the accumulation of clinopyroxene and kaersutite phenocrysts seems insignificant in the latter. In favour of the hypothesis (1) is the fact that olivine and Fe–Ti oxides could have fractionated during the melt ascent. The olivine is mentioned as pseudomorphs (Velde and Tournon 1970; Ubide et al. 2012) in these rocks and its fractionation would explain the low Ni abundances (Fig. 10a); Fe–Ti oxides are also frequent and their earlier crystallization would account for the positive correlation between Mg# and SiO_2 (Fig. 9f). However, since fractional crystallization processes could not consistently explain all the compositional relationships between the two types of camptonites, we suggest that the hypothesis (2) could be feasible. In this model, the two types of camptonites may result either from partial melting of a slightly heterogeneous mantle source or from the variable degree of involvement of specific minerals in the melting process. This would be consistent with the different Nb/Pb ratios of the two types of camptonites (Tab. 5). Moreover, the fact that the potassic camptonites show both the lowest SiO_2 concentrations and Mg# values, together with the highest K#, Rb/Sr and Nb/Pb ratios, could be explained by greater participation of the incongruent breakdown of calcic amphibole and phlogopite during their genesis, which are both undersatured minerals. All these elements are incompatible with calcic amphibole, although Rb and Pb can be more incompatible than Sr and Nb (Tiepolo et al. 2007). In the case of phlogopite, Rb is compatible, whereas Sr, Nb and Pb are incompatible (LaTourrette et al. 1995; Green et al. 2000), but Pb is more incompatible than Nb (LaTourrette et al. 1995). The breakdown of both hydrous mafic phases, for instance according to the reactions amphibole + clinopyroxene = olivine + melt (Médard et al. 2006) or phlogopite = olivine + melt, in the 10–30 kbar pressure range (Yoder and Kushiro 1969), would have relatively enriched the resulting melt in those elements preferentially partitioned by these minerals (e.g., Rb and Nb). This would explain the slightly higher Rb/Sr and Nb/Pb ratios of the potassic camptonites with respect to the sodi–potassic ones. Also in this model, the low values of Mg# and Ni (Fig. 10a) could have resulted from the fact that Mg and Ni would

have been captured by olivine as reaction product of the breakdown of amphibole and phlogopite. Fe–Ti oxides in the mantle residuum may also account for the negative correlation between TiO_2 and SiO_2 among the sodi-potassic camptonites (Fig. 9e).

Rossy et al. (1992) considered LREE- enriched mantle sources for the Cretaceous alkaline magmatism of the Pyrenees, probably situated beneath the lithosphere. This type of protolith, also with residual garnet, would explain the fractionation observed between LREE and HREE (La/Yb_N = 16–18) and among HREE in the studied camptonites (Fig. 11; Gd/Yb_N = 3–4). The more leucocratic segregations could either represent small coalesced portions of the most differentiated, less dense residual melt rising through the unconsolidated camptonite, or resulted from silicate–silicate liquid immiscibility, as the ocelli (Rock 1991 and references therein; Scarrow et al. 2011). The geochemical effects of any of these later processes, or of late degassing, are difficult to discern with the geochemical data of this study. Nonetheless, the ratios between elements with different degrees of mobility are very similar in all camptonites (eg., La/Th = 10–11, Ba/Th = 100–143, Th/U = 3.0–3.5; Tab. 5), and comparable to values of the Primitive Mantle (McDonough and Sun 1995), except for the Ba/Th ratio (83). The higher Ba/Th values in both types of camptonites could be caused either by late or post-magmatic processes or by the breakdown of phlogopite during partial melting since Ba is highly compatible in respect to this mineral (Green et al. 2000; Downes et al. 2004).

9. Conclusions

The multiple intrusion of Platja Fonda was formed by successive magmatic pulses of camptonites emplaced along a fracture system. This outcrop is the northern part of a long sub-horizontal dyke striking N–S to NW–SE.

The camptonites are aphyric and porphyritic, the latter occurring mainly in the central parts of the largest sills. The macrocrysts are interpreted as phenocrysts crystallising during the magma ascent. They are mainly kaersutite with subordinate diopside–augite. These minerals also form microliths in the groundmass along with plagioclase and alkali feldspars. A greater amount of feldspars can be found concentrated in segregations.

The camptonites are slightly potassic and sodi–potassic. Other differences between them are minimal. The potassic type shows the lowest SiO_2 and the highest CaO abundances of all camptonites in the Catalan Coastal Ranges. Also, both types show low Mg # and transition element abundances. There is neither evidence for a simple link by fractional crystallization processes between the two types of camptonite, nor for crustal contamination. Instead, the camptonites may have resulted from partial melting of a metasomatized mantle, in equilibrium with garnet. The incongruent breakdown of calcic amphibole and phlogopite could have been more significant during the genesis of the potassic camptonites.

Acknowledgements. Financial support for this study was provided by the Spanish MINCINN research project CGL2011-26700. We are very grateful to Anikó Batki, and an anonymous reviewer, whose detailed revisions were very helpful in improving the manuscript. We are also indebted to the journal editors, František Holub and Vojtěch Janoušek, for their thoughtful remarks and comments and for the final edition of the manuscript.

References

Adam J, Green T (1994) The effect of pressure and temperature on the partition of Ti, Sr and REE between amphibole, clinopyroxene and basanitic melts. Chem Geol 117: 219–233

Aoki K, Shiba I (1973) Pyroxenes from lherzolite inclusions of Itinome-gata, Japan. Lithos 6: 41–51

Azambre B, Rossy M, Albarède F (1992) Petrology of the alkaline magmatism from the Cretaceous North-Pyrenean Rift Zone (France and Spain). Eur J Mineral 4: 813–834

Bédard JH (1988) Comparative amphibole chemistry of the Monteregian and White Mountain alkaline suites, and the origin of amphibole megacrysts in alkaline basalts and lamprophyres. Mineral Mag 52: 91–103

Cadman A, Tarney J, Park R (1990) Intrusion and crystallization features in Proterozoic dyke swarms. In: Parker AJ, Rickwood PC, Tucker DH (eds) Mafic Dykes and Emplacement Mechanisms. Balkema, Rotterdam, pp 13–14

Downes H, Beard A, Hinton R (2004) Natural experimental charges: an ion-microprobe study of trace element distribution coefficients in glass-rich hornblendite and clinopyroxenite xenoliths. Lithos 75: 1–17

Droop GTR (1987) A general equation for estimating Fe^{3+} concentrations in ferromagnesian silicates and oxides from microprobe analyses, using stoichiometric criteria. Mineral Mag 51: 431–435

Enrique P (1990) The Hercynian intrusive rocks of the Catalonian Coastal Ranges (NE Spain). Acta Geol Hisp 25: 39–64

Enrique P (2009) Las espesartitas, camptonitas y bostonitas del complejo intrusivo de Aiguablava (Cadenas Costero Catalanas): cartografía y composición. Geogaceta 47: 125–128

Enrique P, Butjosa L, Esteve S (2012) Estudio cartográfico de los diques compuestos y multi-intrusivos de lamprófidos del sector oriental del Plutón de Aiguablava. Geo-Temas 13, pp 1–6

Ferrés M (1998) Le complexe granitique alcalin du massif du Cadiretes (Chaînes Côtières Catalanes, NE de l'Espagne): étude pétrologique et géocronologie $^{40}Ar/^{39}Ar$ et Rb–Sr. Unpublished PhD Thesis, Université de Genève, Terre & Environnement 13: pp 1–198

Green TH, Blundy JD, Adam J, Yaxley GM (2000) SIMS determination of trace element partition coefficients between garnet, clinopyroxene and hydrous basaltic liquids at 2–7.5 GPa and 1080–1200 °C. Lithos 53: 165–187

Jerram D, Martin V (2008) Understanding crystal populations and their significance through the magma plumbing system. In: Annen C, Zellmer GF (eds) Dynamics of Crustal Magma Transfer, Storage and Differentiation. Geological Society of London Special Publications 304: 133–148

Julivert M, Fontboté JM, Ribeiro A, Conde LF (1972) Mapa tectónico de la Península Ibérica y Baleares, escala 1:1.000.000. Instituto Geológico y Minero de España (memoria explicativa), Madrid, pp 1–113

LaTourrette T, Hervig K, Holloway JR (1995) Trace element partitioning between amphibole, phlogopite and basanite melt. Earth Planet Sci Lett 135: 13–30

Leake BE, Woolley AR, Arps CES, Birch WD, Gilbert MC, Grice JD, Hawthorne FC, Kato A, Kisch HJ, Krivovichev VG (1997) Nomenclature of amphiboles: report of the Subcommittee on Amphiboles of the International Mineralogical Association, Commission on New Minerals and Mineral Names. Amer Miner 82: 219–246

Le Bas MJ, Le Maitre RW, Streckeisen A, Zanettin B (1986) A chemical classification of volcanic rocks based on the total alkali–silica diagram. J Petrol 27: 745–750

Le Maitre RW (1976) Some problems of the projection of chemical data into mineralogical classifications. Contrib Mineral Petrol 56:181–189

Le Maitre RW, Streckeisen A, Zanettin B, Le Bas MJ, Bonin B, Bateman P, Bellieni G, Dudek A, Efremova S, Keller J, Lameyre J, Sabine PA, Schmid R, Sørensen H, Woolley AR (2002) Igneous Rocks. A Classification and Glossary of Terms. Cambridge University Press, Cambridge, pp 1–236

Losantos M, Montaner J, Solà J, Mató E, Enrique P, Ferrés M, Solé J (2000) Mapa Geològic de Catalunya 1: 25.000, Palafrugell 335-1-1 (79-25). Generalitat de Catalunya ICC

Martínez-Poza AI, Druget E, Castaño LM, Carreras J (2012) The Aiguablava dyke swarm from a structural point of view. Geo-Temas 13: 1–4

McDonough WF, Sun S-s (1995) The composition of the Earth. Chem Geol 120: 223–253

Médard E, Schmidt MW, Schiano P, Ottolini L (2006) Melting of amphibole-bearing wehrlites and experimental study on the origin of ultra-calcic nepheline normative melts. J Petrol 47: 481–504

Montigny R, Azambre B, Rossy M, Thuizat R (1986) K–Ar study of Cretaceous magmatism and metamorphism in the Pyrenees: age and length of rotation of the Iberian Peninsula. Tectonophysics 129: 257–273

Morimoto N, Fabries J, Ferguson AK, Ginzburg IV, Ross M, Seifert FA, Zussman J, Aoki K, Gottardi G (1988) Nomenclature of pyroxenes. Amer Miner 73: 1123–1133

Nicholson R, Pollard D (1985) Dilation and linkage of echelon cracks. J Struct Geol 7: 583–590

Nimis P (1999) Clinopyroxene geobarometry of magmatic rocks. Part 2. Structural geobarometers for basic to acid, tholeiitic and mildly alkaline magmatic systems. Contrib Mineral Petrol 135: 62–74

Nimis P, Ulmer P (1998) Clinopyroxene geobarometry of magmatic rocks. Part 1. An expanded structural geobarometer for anhydrous and hydrous basic and ultrabasic systems. Contrib Mineral Petrol 133: 122–135

Orejana D, Villaseca C, Billström K, Paterson BA (2008) Petrogenesis of Permian alkaline lamprophyres and diabases from the Spanish Central System and their geodynamic context within western Europe. Contrib Mineral Petrol 156: 477–500

Otten MT (1984) The origin of brown hornblende in the Artfjället gabbro and dolerites. Contrib Mineral Petrol 86: 189–199

Pouchou JL, Pichoir F (1984) A new model for quantitative X-ray microanalysis. Rech Aerosp 3: 167–192

Robinson P, Spear FS, Schumacher JC, Laird J, Klein C, Evans BW, Doolan BL (1982) Phase Relations of Metamorphic Amphiboles: Natural Occurrence and Theory. In: Veblen DR, Ribbe PH (eds) Amphiboles: Petrology and Experimental Phase Relations. Mineralogical Society of America Reviews in Mineralogy 9B:1–228

Rock NMS (1991) Lamprophyres. Blackie, Glasgow, pp 1–285

Rossy M, Azambre B, Albarède F (1992) REE and Sr–Nd isotope geochemistry of the alkaline magmatism from the Cretaceous North Pyrenean Rift Zone (France–Spain). Chem Geol 97: 33–46

San Miguel Arribas A (1952) Observations pétrologiques sur les roches lamprophyriques de la Costa Brava Catalogne (Bagur). Congrès Géologique International. C R dixneuvième session, VI, Alger, pp 77–99

San Miguel de la Cámara M (1936) Estudio de las rocas eruptivas de España. Mem R Acad Cienc Exactas, Fis Nat Madrid, Ser Cienc Nat 6: pp 1–660

Scarrow JH, Molina JF, Bea F, Montero P, Vaughan APM (2011) Lamprophyric dykes as tectonic markers of late orogenic transtension timing and kinematics: a case study from the Central Iberian Zone. Tectonics 30: p TC4007

Shimizu N (1990) The oscillatory trace element zoning of augite phenocrysts. Earth Sci Rev 29: 27–37

Shore M, Fowler AD (1996) Oscillatory zoning in minerals: a common phenomenon. Canad Mineral 34: 1111–1126

Smith J, Brown W (1988) Feldspar Minerals. Springer-Verlag, Berlin, pp 1–828

Solé J, Pi T, Enrique P (2003) New geochronological data on the Late Cretaceous alkaline magmatism of the northeast Iberian Peninsula. Cretaceous Res 24: 135–140

Tiepolo M, Oberti R, Zanetti A, Vannucci R, Foley SF (2007) Trace element partitioning between amphibole and silicate melt. In: Rosso JJ (ed) Amphiboles: Crystal Chemistry, Occurrence and Health Issues. Mineralogical Society of America Reviews in Mineralogy and Geochemistry 67: 417–452

Ubide T, Galé C, Arranz E, Lago M (2008) Composition of the Aiguablava camptonite sill (Costa Brava Batholith). Macla 9: 249–250

Ubide T, Arranz E, Galé C, Lago M (2009) Variación vertical de la composición de un sill de lamprófido: influencia de fases xenocristalinas. Macla 11: 191–192

Ubide T, Lago M, Arranz E, Galé C, Larrea P (2010) The lamprophyric sub-vertical dyke swarm from Aiguablava (Catalonian Coastal Ranges): petrology and composition. Geogaceta 49: 83–86

Ubide T, Arranz E, Lago M, Galé C, Larrea P (2012) The influence of crystal settling on the compositional zoning of a thin lamprophyre sill: a multi-method approach. Lithos 132: 37–49

Velde D, Tournon J (1970) Le camptonite de San Feliu de Buxalleu (Province de Gérone, Espagne). Bull Soc Fr Minéral Cristallogr 93: 482–487

Whitney DL, Evans BW (2010) Abbreviations for names of rock forming minerals. Amer Miner 95: 185–187

Yoder Jr HS, Kushiro I (1969) Melting of hydrous phases: phlogopite. Amer J Sci 267: 558–582

Yoder Jr HS, Tilley CE (1962) Origin of basalt magmas: an experimental study of natural and synthetic rock systems. J Petrol 3: 342–532